Superconducting and structural properties of the noncentrosymmetric Re_6Hf superconductor under high pressure

Sathiskumar Mariappan,[1,2] Manikandan Krishnan,[1] Dilip Bhoi,[2] Hanming Ma,[2] Jun Gouchi,[2] Kapil Motla,[3] R. P. Singh,[3] Ponniah Vajeeston,[4] Arumugam Sonachalam,[1,*] and Yoshiya Uwatoko[2,†]

[1]*Centre for High Pressure Research, School of Physics, Bharathidasan University, Tiruchirappalli, 620024, India*
[2]*Institute for Solid State Physics, The University of Tokyo, 5-1-5 Kashiwanoha, Kashiwa, Chiba, 277–8581, Japan*
[3]*Indian Institute of Science Education and Research Bhopal, Bhopal, 462066, India*
[4]*Department of Chemistry, Centre for Materials Science and Nanotechnology, University of Oslo, P.O. Box 11126, Blindern, N-0318 Oslo, Norway*

(Received 18 January 2022; revised 20 April 2022; accepted 11 May 2022; published 6 June 2022)

We report the effect of high pressure on the superconducting, vortex pinning, and structural properties of a polycrystalline, noncentrosymmetric superconductor Re_6Hf. The superconducting transition temperature, T_c, reveals a modest decrease as pressure (P) increases with a slope of -0.046 K/GPa (-0.065 K/GPa) estimated from resistivity measurements up to 8 GPa (magnetization measurement $\sim$1.1 GPa). Structural analysis up to $\sim$18 GPa reveals monotonic decreases of lattice constant without undergoing any structural transition and a high value of bulk modulus $B_0 \approx 333.63$ GPa, indicating the stability of the structure. Furthermore, the upper critical field and lower critical field at absolute temperature [$H_{c2}(0)$ and $H_{c1}(0)$] decrease slightly from the ambient pressure value as pressure increases up to 2.5 GPa. In addition, analysis of $\rho(T, H)$ up to $P \sim 2.5$ GPa using thermally activated flux flow of vortices revealed a double linearity field dependence of activation energy of vortices [$U_o(H)$], confirming the coexistence of single and collective pinning vortex states. Moreover, analysis of critical current density using the collective pinning theory showed the transformation of δT_c to δl pinning as pressure increases, possibly due to migration of grain boundaries. Besides, the band structure calculations using density functional theory show that density of states decreases modestly with pressure, which may be a possible reason for such a small decrease in T_c by pressure.

DOI: 10.1103/PhysRevB.105.224505

I. INTRODUCTION

The discovery of superconductivity in noncentrosymmetric (NCS) compounds, which lack inversion symmetry, has encouraged theoretical and experimental investigations because these compounds can host unconventional superconductivity. For example, the magnetic NCS superconductor $CePt_3Si$ has shown the signature of mixed parity states involving spin-singlet and triplet Cooper pairs in the superconducting state [1,2]. However, the superconducting pairing glue forming the Cooper pair in these NCS compounds, such as $CePt_3Si$ [1,3], Ce(Rh, Ir)Si_3 [4,5], and Ce(Co, Ir)Ge_3 [6,7], is complicated by the coexistence of magnetic order and superconductivity. Moreover, when such heavy fermionic NCS compounds are pressurized, the long-range magnetic order is continuously suppressed and superconductivity appears in a wide P range [5,8–13]. Similarly, in both $CePdSi_2$ and $CeIn_3$ antiferromagnetic order decreased monotonically, followed by the appearance of superconductivity above critical pressure (P_c) [14]. Unlike these magnetic compounds, numerous nonmagnetic NCS superconducting compounds, such as $LaNiC_2$ ($T_c \sim 2.8$ K) [15,16], $Li_2(Pd, Pt)_3B$ ($T_c \sim$ 7 K and 2.7 K) [17,18], (Ta,Nb)Rh_2B_2 ($T_c \sim 6$ K and 7.6 K) [19–21], BiPd ($T_c \sim 3.8$ K) [22,23], and SrPtAs ($T_c \sim 2.4$ K $\sim$2.4 K) [24,25], have also been studied and found to exhibit the unconventional nature of superconductivity.

Apart from these compounds, in recent years we have seen a quick development in both experimental and theoretical studies on new Re-based nonmagnetic NCS compounds such as Re_6(Zr,Ti) ($T_c \sim 6.75$ K and 6 K) [26–28], Re_3Ta ($T_c \sim$ 4.68 K) [29], $Re_{24}Ti_5$ ($T_c \sim 6$ K) [30,31], and $Re_{0.82}Nb_{0.18}$ ($T_c \sim 8.8$ K) [32,33]. The $H_{c2}(0)$ of these NCS compounds is very close to the Pauli paramagnetic limit, $H_p \sim 1.86 \times T_c$. Besides, the temperature dependence of heat capacity below T_c is well explained by the s-wave symmetry of the Cooper pairs [28,30]. Although these results are consistent with the expectations for a conventional BCS-type superconductor, muon spin rotation (μSR) experiments have revealed the signature of time-reversal symmetry breaking in Re_6X (X = Zr, Ti, Hf) [26,27,34]. Furthermore, Re_6Hf has shown type-II superconductivity with the signature of possible mixing of spin-singlet and triplet states [34].

Besides the investigation of superconducting properties at ambient pressure, there are a few reports on the effects of chemical pressure as well as external pressure on the superconducting properties of Re_6Hf [35]. On substituting Fe in place of Re, T_c of Re_6Hf is suppressed rapidly, suggesting that the superconductivity is drastically affected by the

*Corresponding author: sarumugam1963@yahoo.com
†Corresponding author: uwatoko@issp.u-tokyo.ac.jp

doping of magnetic impurities. In contrast, by the application of external P up to 2.5 GPa, the T_c of Re_6Hf shows little change [35]. Very recently, good-quality polycrystalline samples of Re_6Hf have been synthesized via the arc-melting technique, and the structural and superconducting properties were reported [36]. In this work, using high-quality polycrystalline Re_6Hf samples, we have studied the effect of pressure on the structural and electronic properties of Re_6Hf via transport (∼8 GPa), magnetic (∼1 GPa), and powder x-ray diffraction (XRD) (∼18.01 GPa) measurements. In addition, complementary density functional theory (DFT) calculations (up to ∼25 GPa) have also been performed in order to understand the mechanism of superconductivity.

II. EXPERIMENTAL TECHNIQUES

High-quality polycrystalline Re_6Hf compound is prepared via the arc-melting technique as described in Ref. [36]. The details of the phase purity and sample characterization at ambient pressure are reported in Ref. [36]. The temperature-dependent electrical resistivity [$\rho(T)$] was measured at ambient pressure with high magnetic field using an Oxford 18 Tesla magnet and AC resistance bridge. Also, $\rho(T)$ were measured by the standard four-probe method using the physical properties measurement system (PPMS). $\rho(T)$ with the presence of a magnetic field (H) were measured at ambient and high pressure up to ∼2.5 GPa using a double-layer self-clamp-type piston pressure cell which is made of Be-Cu and Ni-Cr-Al alloys. The pressure-transmitting medium was Daphne Oil 7474 for its adequate hydrostatic nature to measure the electrical resistivity of synthesized compounds. The actual pressure inside the pressure cell was determined using the superconducting T_c of a Pb specimen. A cubic anvil-type device was used to measure $\rho(T)$ for $P \sim 2$ to 8 GPa at the Institute of Solid State Physics, University of Tokyo, Japan. It consists of six tungsten carbide (WC) anvils to generate homogeneous hydrostatic pressure on the sample. The sample was placed in a Teflon capsule which was filled with the pressure medium (Daphne 7474), and then the Teflon cell was fixed in the pyrophyllite gasket and the gasket placed between the six WC anvils. The electrical contacts were made using gold wire of $\phi \sim 20\,\mu$m and Ag paste. The applied pressure was calibrated using resistive transitions of Bi I-II (2.55 GPa), Bi II-III (2.7 GPa), and Bi III-IV (7.7 GPa) at room temperature [37]. The temperature- and field-dependent magnetization measurements were measured using a magnetic property measurement system (MPMS-XL, Quantum Design, USA) at ambient and high P. The rectangular-shaped sample with the dimensions of length (l) ≈ 0.281 cm, width (b) ≈ 0.105 cm, and thickness (t) = 0.042 cm was used for all magnetic measurements. The magnetic field was applied parallel to the length of the sample. External applied P up to ∼1 GPa was produced by a clamp-type micropressure cell made of nonmagnetic Cu–Be alloy. The Daphne 7474 was used as a pressure-transmitting medium, and the actual pressure was calibrated from the P dependence of superconducting T_c of Sn. The high-pressure XRD patterns were recorded by a Rigaku, XtaLab HyPixsel 6000 diffractometer with Mo $K\alpha$ radiation ($\lambda = 0.71073$ Å) at room temperature used for obtaining the diffraction pattern of a single crystal. The obtained data were converted into intensity vs 2θ pattern using the CRYSALIS PRO software. Pressure was generated using a diamond anvil cell (DAC) with rhenium as a gasket (thickness 70 μm, hole $\phi = 0.1$ mm). A mixture of methanol and ethanol (1:1) was used as a pressure-transmitting medium, and the pressure was calibrated from ruby by the luminescence method. The emission signals (R_1 and R_2) of the ruby sample are received from other side of the cell through the gasket hole.

III. COMPUTATIONAL DETAILS

The computations were carried out in the context of periodic density functional theory, as implemented in the VASP code [38] and examined using Re_6Hf, which exhibits the $I\bar{4}3m$ space group. The interaction of the core (Re:[Xe] and Hf: [Xe]) and valence electrons has been characterized using the projector-augmented wave (PAW) approach [39,40]. For the structural optimization, we used the Perdew, Burke, and Ernzerhof (PBE) gradient corrected functional for the exchange-correlation part of the potential. Our earlier [41] computations indicated that the only way to forecast structural characteristics in superconducting materials properly is to use a strong energy cutoff to ensure basis-set completeness. As a result, we chose a cutoff of 600 eV. When all atomic forces were less than 0.02 eV Å^{-1}, it was presumed that the atoms were relaxed, and the geometries were optimized when the total energy converged to less than 1 meV between two successive geometric optimization steps. The electronic characteristics of the structures optimized at the PBE level were computed. The following section discusses the reliability of this computational approach. We employed a Monkhorst–Pack $9 \times 9 \times 9$ k mesh for structural optimization and electrical structure research unless otherwise noted. The band structures of the irreducible part of the first Brillouin zone were determined by solving the periodic Kohn–Sham equation at ten k points along each direction of high symmetry. Total energy as a function of volume has been computed and fitted using the universal equation of state (EOS) [42]. Pressure vs Gibbs free energy curves are used to compute the transition pressures. Gibbs free energy ($G = U + PV - TS$; G = total energy + pressure × volume) is determined as follows: The volume vs total energy curve is fitted to the universal EOS function $P = (\frac{B_0}{B_0'}) \times [(\frac{v_e}{v})^{B_0'} - 1]$. The relationship can be inverted to obtain the volume $(v) = v_e/[(1 + (\frac{B_0'}{B_0}) \times P)^{\frac{1}{B_0'}}]$, where, respectively, v_e, B_0, and B_0' denote the equilibrium volume, the bulk modulus, and its pressure derivative. Following that, the bisection method is used to calculate the inverse. The enthalpy difference between the two data sets was computed using the scan over the pressures. According to the fitted energy-volume curve, the computed B_0 is 270 GPa and the B_0' is 3.83.

Re_6Hf has approximately eight formula units per unit cell and is fundamentally disordered. Hf inhabited both 2a (0,0,0) and 8c (0.3106,0.3106,0.3106) sites, while Re occupied two 24g (0.3623,0.3623,0.0383) and 24g (0.6954,0.6954,0.2903) sites [36]. The composition of the fully stoichiometric phase is $Re_{48}Hf_{10}$, with Hf occupancy of 80%. The *ab initio* random searching structure (AIRSS) [43] approach was used to

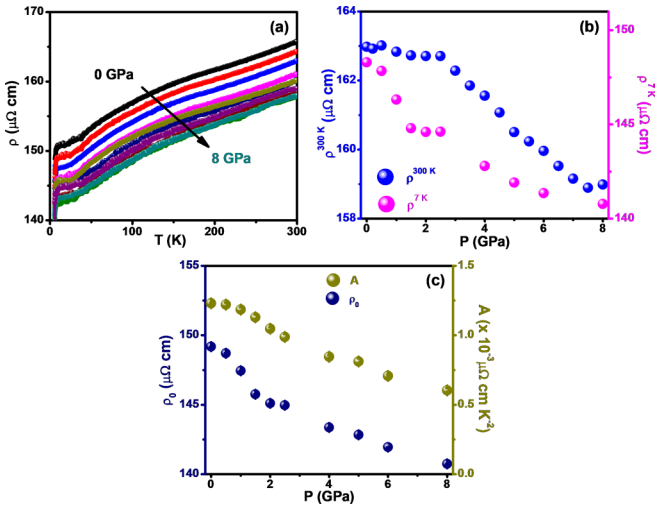

FIG. 1. (a) Normal-state $\rho(T)$ under various applied hydrostatic pressures, (b) P dependence of resistivity at room temperature and 7 K ($\rho_{300\ K}$ and $\rho_{7\ K}$). (c) P dependence of ρ_0 and scattering factor (A) determined from Fermi-liquid model fitting $\rho = \rho_0 + AT^2$.

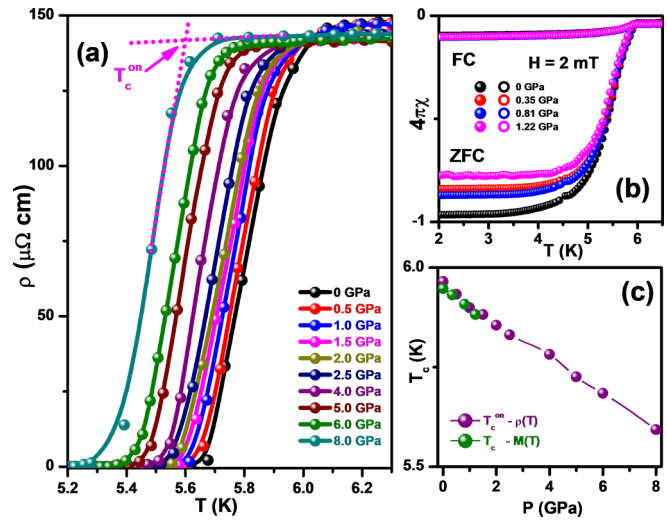

FIG. 2. (a) $\rho(T)$ under various applied hydrostatic pressures near superconducting T_c region, (b) temperature dependence of unitless magnetic susceptibility [$\chi(T)$] with a magnetic field of 2 mT for Re_6Hf, and (c) P dependence of onset of superconducting T_c from $\rho(T)$ and $\chi(T)$ measurements for Re_6Hf.

generate alternative model structures for the specified substitution in the $Re_{48}Hf_{10}$ matrix, in addition to VASP calculations, for the partial occupancy simulation. As a result, Hf has been substituted for the vacancy in the acquired AIRSS model, and the structure has been completely relaxed. In this scenario, the composition of the theoretical sample (Re_6Hf) is almost identical to the composition of the experimental sample.

IV. RESULTS AND DISCUSSION

Figure 1(a) shows the $\rho(T)$ of Re_6Hf under various applied pressure (P) up to ~8 GPa. The sharp superconducting transition and zero resistivity at each pressure indicate the hydrostatic pressure is maintained during the whole set of measurements. At ambient pressure, as temperature decreases ρ decreases, from 163 $\mu\Omega$ cm at 300 K to 148.3 $\mu\Omega$ cm at 7 K [as shown in Fig. 1(b)]. The residual resistivity ratio, defined as $\rho_{300\ K}/\rho_{7\ K} \sim 1.14$, is rather small due to the disorder dominated in this system and is similar to other Re-based NCS compounds [29,31,33,36]. With the application of pressure, the overall $\rho(T)$ slightly decreases. As P increases from 0 to 8 GPa, $\rho_{300\ K}$ decreases linearly with a slope of $-0.11\ \mu\Omega$ cm/GPa ($0 \leqslant P \leqslant 2.5$ GPa) thereafter follows a faster rate of decrease $\sim 0.63\ \mu\Omega$ cm/GPa. To further understand the normal-state properties, we analyzed the $\rho(T)$ in the temperature range 10 K $\leqslant T \leqslant$ 50 K at various P using the Fermi-liquid relation, $\rho = \rho_0 + AT^2$, where ρ_0 and A are residual resistivity and electron-electron scattering factor, respectively. As shown in Fig. 1(c), ρ_0 decreases from 149.18 $\mu\Omega$ cm at ambient pressure to 140.75 $\mu\Omega$ cm at 8 GPa. Simultaneously, A decreases from 1.25 $\mu\Omega\,\mathrm{cm/K^2}$ at ambient pressure to $0.60 \times 10^{-3}\ \mu\Omega\ \mathrm{cm/K^2}$ at 8 GPa. The small value of A suggests that Re_6Hf is a weakly correlated system.

To see the evolution of superconductivity under pressure, we plotted the $\rho(T)$ near the superconducting transition region at various pressures in Fig. 2(a). The $\rho(T)$ transition shifts parallel towards low temperature with pressure. We estimated the onset of the superconducting transition temperature, T_c^{on}, from the intersection of two extrapolated lines. One is drawn through the normal-state $\rho(T)$ curve and the other is drawn through the superconducting transition region as shown in Fig. 2(a). At ambient pressure, T_c^{on} ~5.96 K and the zero-resistivity temperature T_c^0 ~5.56 K. The superconducting transition width, $\Delta T_c = T_c^{\mathrm{on}} - T_c^0 \approx$ 0.40 K at 0 GPa, is rather sharp and comparable to a previous report [36]. With pressure, T_c^{on} decreases to 5.59 K at 8.0 GPa and $\Delta T_c \sim 0.22$ K becomes sharper. Figure 2(b) shows temperature-dependent zero-field-cooled (ZFC) and field-cooled (FC) magnetic susceptibility ($4\pi\chi$), measured with an applied magnetic field 2 mT from 0 to ~1.2 GPa. The estimated $4\pi\chi$ at 2 K reaches -0.96, suggesting the full Meissner state at ambient pressure. The $4\pi\chi$ decreases to -0.77 at 1.22 GPa, indicating the reduction of Meissner fraction with increasing P. The ZFC magnetic curve displays a transition at T_c^{on} ~5.95 K at 0 GPa and 5.88 K at 1.2 GPa, which is in good agreement with the T_c determined from $\rho(T)$ for $P < 1.5$ GPa. In Fig. 2(c), using the magnetization (up to ~1.2 GPa) and resistivity (up to ~8 GPa), we summarized the T_c vs P curve for Re_6Hf, revealing a monotonic decrease of T_c with P. The rate of suppression of T_c with respect to the applied P, dT_c/dP, determined from $\rho(T, P)$ is ~ -0.046 K/GPa, whereas from $\chi(T)$ it shows a slightly faster decrease, $dT_c/dP \sim -0.065$ K/GPa.

Figures 3(a)–3(d) show the magnetic field dependence of isothermal magnetization, $M(H)$, at various temperatures with different fixed applied P of 0 GPa, 0.35 GPa, 0.81 GPa, and 1.22 GPa, respectively. (Detailed $M(H)$ curves are given in the Supplemental Material [44].) In both ambient and high P, a linear response of the Meissner signal can be clearly seen in the $M(H)$ curve in the low-magnetic-field region. From the $M(H)$ curves, we determined the temperature dependence of the lower critical field, $H_{c1}(T)$, as the field where the Meissner signal deviates from linearity, as shown in Fig. 3(a). The

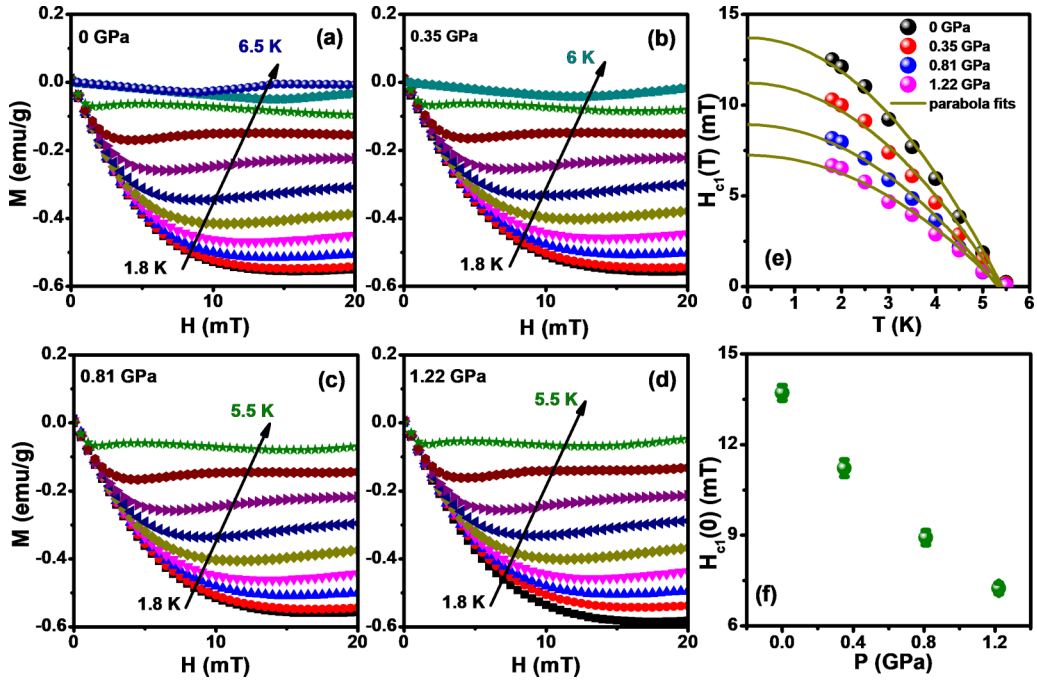

FIG. 3. (a)–(d) $M(H)$ at various temperatures under constant P of 0 GPa, 0.35 GPa, 0.81 GPa, and 1.22 GPa. (e) $H_{c1}(T)$ at fixed P, and the solid lines represent the GL relation. (f) P dependence of $H_{c1}(0)$ estimated from the GL relation fits for Re_6Hf.

deflection observed in isothermal magnetization curves is more noticeable and its slope is given by $M = \frac{-H_\alpha}{1-N}$, where H_α is the external applied field and N is the demagnetization factor. For an ellipsoidal sample, N is given by the relation $N = (\frac{2}{\pi})arc\ \sin(1/[1+2(\frac{l}{b})])$, with l and b as the length and width of the samples, respectively [45]. We also calculated the N assuming a prismatic-shaped sample based on the relation $N = bc/(ab+bc+ca)$ [46]. For both methods we obtained rather a small value of N (~ 0.07 for an ellipsoidal sample and ~ 0.09 for a prismatic-shaped sample). These small values of N suggest that the demagnetization factor will not severely affect the overall analysis. The obtained $H_{c1}(T)$ fit with the quadratic Ginzburg-Landau (GL) relation [47], $H_{c1}(T) = H_{c1}(0)[1-(\frac{T}{T_c})^2]$ and is shown in Fig. 3(e). From the GL fitting, $H_{c1}(0)$ is estimated to be 5.88 mT at 0 GPa and found to decrease to 5.52 mT at 1.22 GPa, as shown in Fig. 3(f).

To determine the $H_{c2}(0)$, we measured the $\rho(T)$ by fixing the magnetic fields [shown in Figs. 4(a)–4(i)] as well as the field dependence of resistivity [$\rho(H)$] by fixing the temperature across the superconducting region at ambient and high P [shown in Figs. 4(f)–4(i)]. The temperature dependence of upper critical field, $H_{c2}(T)$, curve at different pressures is estimated as the magnetic field dependence of T_c^{on} determined from the $\rho(T)$ and $\rho(H)$ data. At ambient P, $\rho(H)$ is found to be zero even up to 10 T above, which changes from superconducting to normal state. In Fig. 5 we plotted the $H_{c2}(T)$ at different pressures. To understand the superconducting pairing mechanism, we analyzed the $H_{c2}(T)$ using the single-band Werthamer-Helfand-Hohenberg (WHH) relation, $H_{c2}^{orb}(0) = 0.693T_c(\frac{dH_{c2}}{dT})_{T_c}$ [48], where $(\frac{dH_{c2}}{dT})_{T_c}$ is the slope of the $H_{c2}(T)$ curve at $T = T_c$ and $H_{c2}^{orb}(0)$ is the orbital pair-breaking critical field at absolute zero. P dependence of $H_{c2}^{orb}(0)$ is found to decrease from 9.78 T at ambient condition to 9.18 T at 2.5 GPa [Fig. 6(a)]. We also estimated the $H_{c2}(0)$ as shown in Fig. 5 using the GL theory, $H_{c2}(T) = H_{c2}^{GL}(0)(\frac{(1-t^2)}{(1+t^2)})$, where t is the normalized temperature T/T_c and $H_{c2}^{GL}(0)$ is the upper critical field at zero temperature. At ambient pressure and high P, we found that $H_{c2}^{GL}(0)$ evaluated by fitting the GL formula is higher than $H_{c2}^{orb}(0)$ [Fig. 6(a)]. From Fig. 6(a), it is also clear that $H_{c2}^{GL}(0)$ is only slightly higher than the Pauli limited upper critical field, $H_p(0)$, while $H_{c2}^{orb}(0)$ is slightly lower than $H_p(0)$. For weakly coupled BCS superconductors [49–51], $H_p(0) = 1.86 \times T_c$, which changes very weakly with P. The comparable values of the upper critical fields $H_{c2}^{orb}(0)$ and $H_{c2}^{GL}(0)$ with that of $H_p(0)$ do not firmly support the existence of spin-triplet pairing in Re_6Hf. But the observation of time-reversal symmetry breaking in recent μSR study does not completely rule out the possibilities of any spin-triplet pairing in Re_6Hf contributing to the superconductivity [34]. Similar comparable values of the upper critical fields, $\mu_0 H_{c2}^{orb}(0)$ and $\mu_0 H_{c2}^{GL}(0)$, to the $H_p(0)$ and their P dependence have also been observed in NCS $TaRh_2B_2$, which has also been investigated as a potential candidate with a spin-triplet pairing [19]. Furthermore, the estimated Maki parameter [52], $\alpha = \sqrt{2}H_{c2}^{orb}(0)/H_p(0) \sim 1.24-1.2$, is higher than 1 [Fig. 6(b)], indicating the significant paramagnetic pair-breaking effect. The superconducting GL coherence length relation is $H_{c2}^{GL}(0) = \Phi_0/2\pi\xi_0^2$, where Φ_0 is flux quantum (2.07×10^{-15} Wb) and P-dependent ξ_0 are shown in Fig. 6(c).

Upon application of a magnetic field, the resistivity in the superconducting transition region broadens and shifts towards a lower temperature due to dissipative thermally activated flux

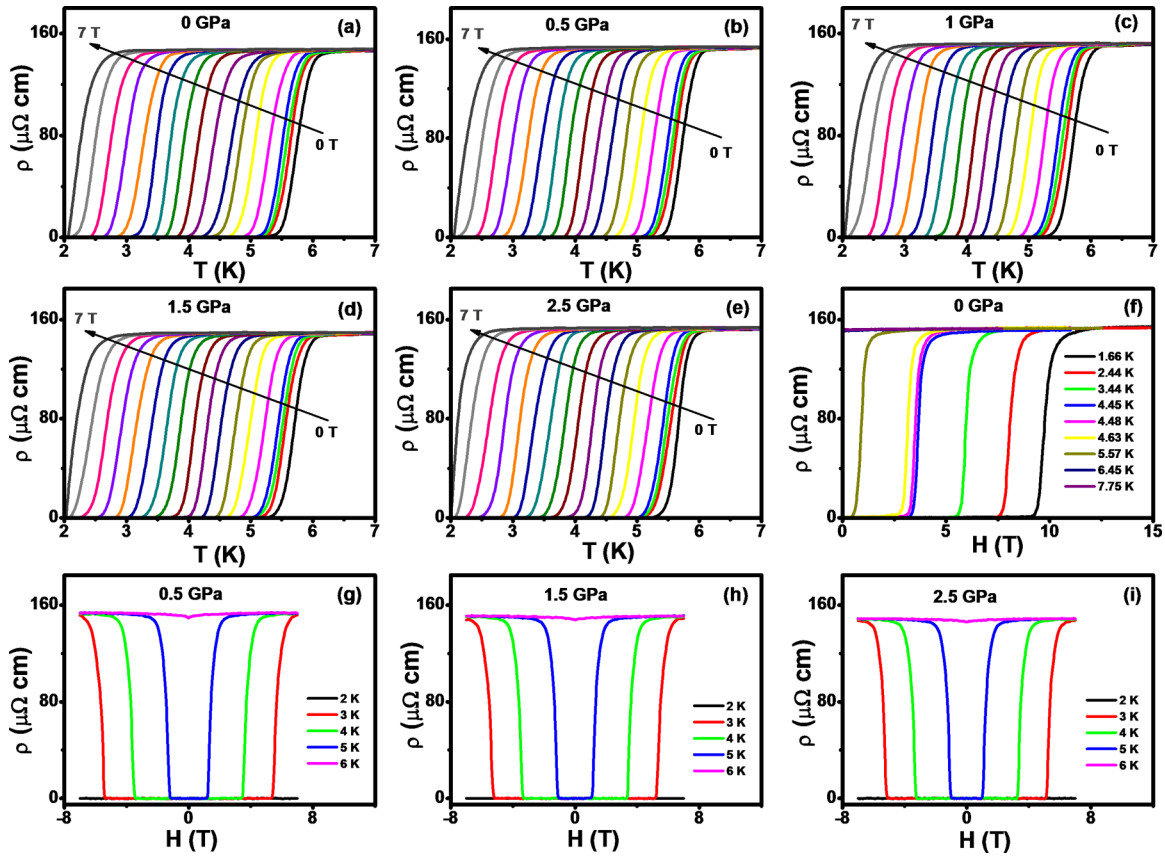

FIG. 4. (a)–(e) $\rho(T)$ at various applied magnetic fields under constant P from 0 to 2.5 GPa. (f)–(i) $\rho(H)$ at various temperatures with applied P of 0 GPa, 0.5 GPa, 1.5 GPa, and 2.5 GPa for Re_6Hf.

flow (TAFF) of vortices. In the TAFF regime, a finite resistivity occurs from the competition between two mechanisms: flux creep (pinning force of vortices) and flux flow (Lorentz force acting on the vortices) [53]. In this region, resistivity follows the Arrhenius expression $\ln(T,H) = \ln\rho_0(H) - \frac{U_0(H)}{T}$, where $\ln\rho_0 = \ln\rho_{0f} + \frac{U_0}{T_c}$, and U_0 is the apparent activation

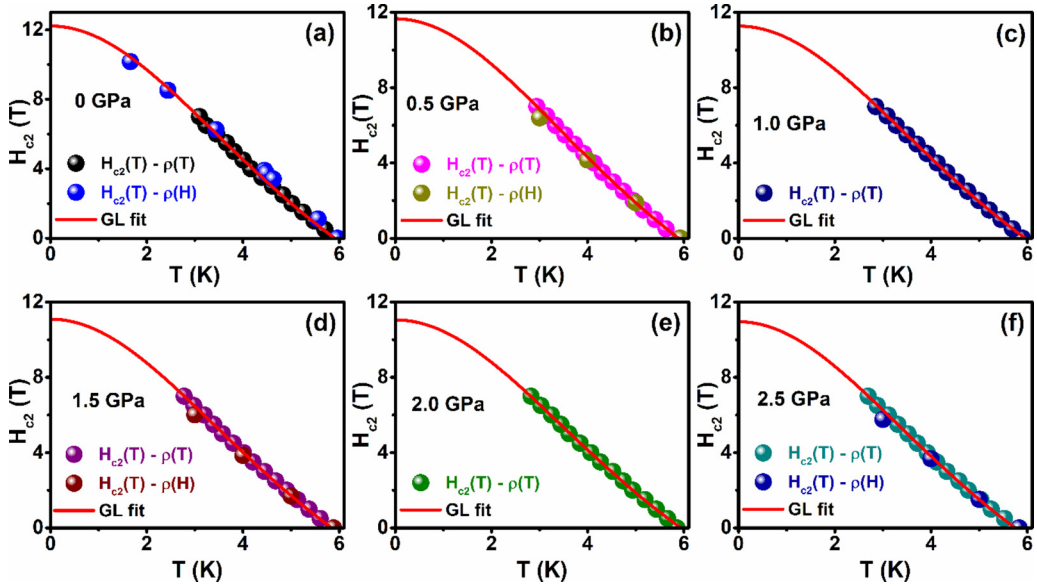

FIG. 5. (a)–(f) $H_{c2}(T)$ determined from $\rho(T,H)$ measurements at various applied P of 0 GPa, 0.5 GPa, 1 GPa, 1.5 GPa, 2 GPa, and 2.5 GPa, and solid lines fitted with G-L relation yields $H_{c2}(0)$ for Re_6Hf.

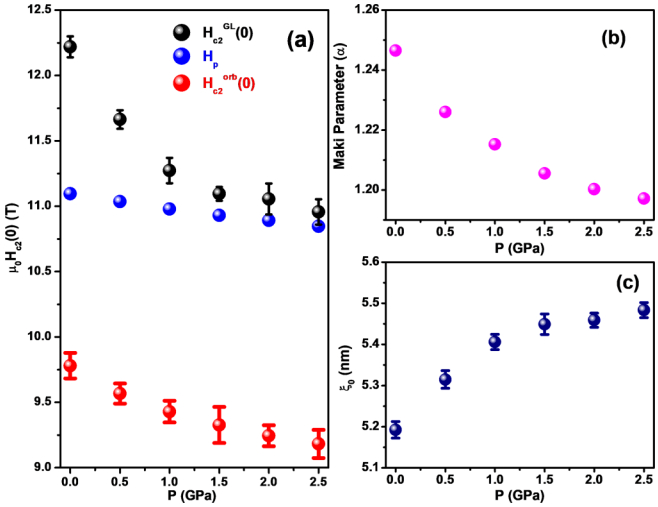

FIG. 6. (a) P dependence of upper critical fields [$\mu_0 H_{c2}^{\mathrm{GL}}(0)$ and $\mu_0 H_{c2}^{\mathrm{orb}}(0)$] and Pauli limited critical field [$\mu_0 H_p(0)$], (b) Maki parameter (α), and (c) coherence length ξ_0 for Re_6Hf.

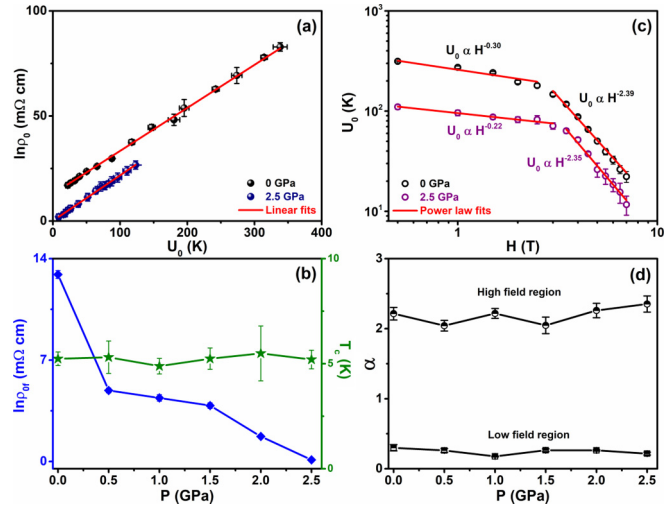

FIG. 7. (a) ln $\rho_0(H)$ vs $U_0(K)$ determined from the Arrhenius graph [log $\rho(T,H)$ vs $1/T$] in different magnetic fields at $P = 0$ and 2.5 GPa for Re_6Hf. (b) P-dependent ln ρ_{0f} and calculated T_c. (c) U_0vs H determined from the Arrhenius plot, log $\rho(T)$ vs $1/T$, in different magnetic fields at $P = 0$ and 2.5 GPa for Re_6Hf. (d) Pressure dependence α value calculated from power-law dependence of $U_0(H) \propto H^{-\alpha}$ at low-field and high-field region of U_0.

energy, which plays a crucial role as an effective pinning barrier of vortices [54]. Both at ambient and high P, on plotting the ln[$\rho(T,H)$] in the TAFF region as function of $1/T$ reveals a linear curve, thus confirming the Arrhenius behavior of resistivity in the TAFF regime. The temperature dependences of thermally activated energy (TAE), U(T,H) is revealed as almost linear as observed from $U = U_0(H)(1-\frac{T}{T_c})$. On extrapolation, the fitted linear lines to the ln $\rho(T,H)$ vs $1/T$ curve at various magnetic fields intersect at a temperature close to superconducting T_c. Moreover, in Fig. 7(a) log $\rho_0(H)$ vs $U_0(H)$ shows a linear behavior and can be fitted with the relation $\ln\rho_0 = \ln\rho_{0f} + \frac{U_0}{T_c}$. The extracted parameters ρ_{0f} and T_c at both ambient and high P are shown in Fig. 7(b). The linear relationship between (U_0) and lnρ_0 for all pressures confirms the validity of our analysis. On increasing P to 2.5 GPa, the values of ρ_{0f} decrease to 5.16 mΩ cm from 12.96 mΩ cm at ambient pressure. T_c also decreases to 5.16 K from 5.26 K at ambient pressure, consistent with the experimental behavior of T_c under P, even though the estimated T_c values are slightly lower. $U_0(H)$ can be extracted from the Arrhenius relation, as $U_0(H) = \partial \ln\rho/\partial(\frac{1}{T})$. In Fig. 7(a) we plotted the $U_0(H)$ at different pressures. From Fig. 7(c) it is clear that U_0 decreases both with the H field dependence of U_0, revealing two different linear regions, suggesting the power-law dependence of $U_0(H) \propto H^{-\alpha}$ and confirming the transition from a single vortex to collective (mixed) vortex state with an increasing field. The low-magnetic-field region is dominated by a single vortex without any possibility for the existence of mixing; therefore $U_0(H)$ reveals a weak magnetic field dependence. With the increasing magnetic field at a singular point, the pinning energy decreases and results in strong magnetic field dependence; this indicates the overlapping of vortices at the high-field region. The sharp decrease of $U_0(H)$ for $H > 2.5\ T$ confirms a crossover from a single to a collective flux pinning regime. As shown in Fig. 7(d), α is found to be $0.30 \leqslant \alpha \leqslant 0.22$ ($H < 2.5$ T) and $2.39 \leqslant \alpha \leqslant 2.35$ ($H > 2.5$ T) as pressure increases to 2.5 GPa. As pressure increases, $U_0(H)$ decreases, which implies that overlapping of both single and collective vortex states as realized in Re_6Hf.

The magnetic field dependence of critical current density, $J_c(H)$, is deduced from $M(H)$ curves for $T < T_c$ at different P. According to Bean's critical model [55,56], for a rectangular-shaped sample, $J_c(H) = \frac{20\Delta M(H)}{l-(l^2-3b)}$, where $\Delta M(H)$ is the width of the superconducting isothermal magnetic loop and l and b are the length and width of the sample, respectively. The $J_c(H)$ at various temperatures are shown in Figs. 8(a) and 8(b) for pressure ranging from 0 to ∼1.10 GPa. With increasing pressure, $J_c(H = 0, 2\ \mathrm{K})$ decreases from 1.1×10^5 A/cm^2 at 0 GPa to 0.64×10^5 A/cm^2 at 1.10 GPa. This decreasing trend of $J_c(H = 0, 2\ \mathrm{K})$ with pressure is similar to many Fe-based and two-dimensional layer [$NbSe_2$, $Ba(Fe_{0.88}Co_{0.12})_2As_2$] superconductors [57–59]. However, $J_c(H = 0, 2\ \mathrm{K})$ for Re_6Hf is several orders of magnitude higher than the high-T_c cuprate superconductors $J_c(H = 0) \sim 10^4$–10^5 [60,61]. To obtain further insight into the nature of the vortex state in Re_6Hf, we analyzed the field dependence of J_c using the collective vortex pinning model. Based on this model, $J_c(H)$ should follow a relation $J_c(H) = J_0 \exp^{[-(H/H_0\frac{H}{H_0})]^{3/2}}$, where J_0 and H_0 are the critical current density at 0 T and controlled parameter, respectively [62]. For all pressures (Fig. 8), $J_c(H)$ at different temperatures can be well described by the above relation, implying the collective pinning of vortices. For further information, we also analyzed the P dependence of J_c at 2 K at different H, as shown in Fig. 8(c). The linear fits to the data suggest that for all fields J_c decreases with increasing pressure at a similar rate $\frac{d[(\log J_c(H,T))]}{dP} = 0.20 \pm 0.03 \frac{\mathrm{A\ cm^{-2}}}{\mathrm{GPa}}$, which could help one to understand the interaction between the vortices and the pinning center. Figure 8(c) shows $J_c(T)$

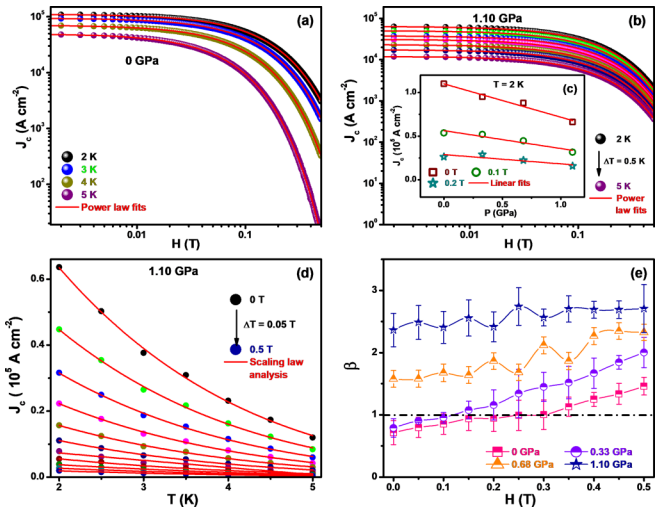

FIG. 8. (a), (b) $J_c(H)$ at different temperatures for $P = 0$ and 1.10 GPa, respectively, for Re_6Hf. Solid lines represent the power-law behavior of the collective pinning model as described in the text. (c) P dependence of $J_c(H)$ at 2 K, solid lines represent the linear fits to the data. (d) Temperature dependence of critical current density J_c at different fields with $P = 1.10$ GPa for Re_6Hf. Solid lines represent the scaling law $[J_c(H) \propto (1-\frac{T}{T_c})^{\beta}]$. (e) Magnetic field dependence of β at different P Dash-dotted line at $\beta = 1$ separates the single and collective vortex region.

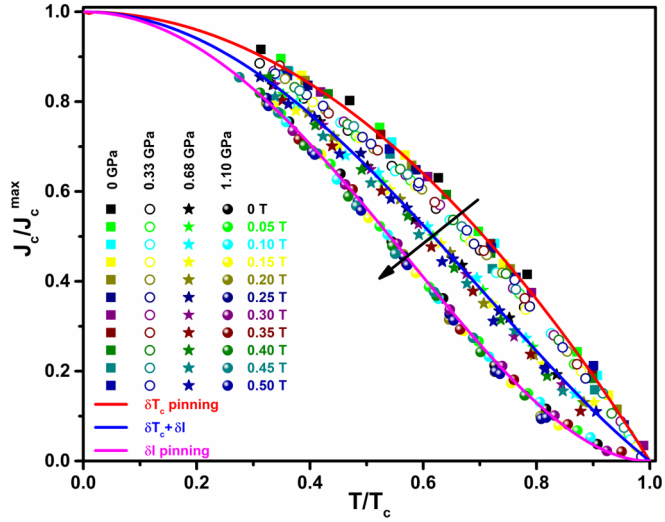

FIG. 9. Normalized temperature dependence of J_c at different magnetic fields with various $P = 0$, 0.33, 0.68, and 1.10 GPa. Solid lines describe the fits to the data for δT_c, $\delta T_c + \delta l$, and δl pinning based on the model of collective vortex pinning.

for different H at 1.10 GPa. Also, information about the nature of the vortex pinning mechanism can be obtained by analyzing the temperature dependence of J_c at a particular magnetic field. Based on Ginzburg-Landau theory, $J_c(T)$ at various H can be fitted with a power-law relation, $J_c(H) \propto (1-\frac{T}{T_c})^{\beta}$. The specific value of the exponent β signifies the vortex pinning mechanism in that magnetic field. For $\beta =\sim 1$ and $\leqslant 1.5$ noninteracting vortices and core pinning mechanisms [63] are indicated, respectively. From Fig. 8(d), it is clear that for P up to 0.33 GPa, β remains less than 1 in the low-field region ($H < 0.15\ T\ -0.25\ T$). However, with a gradual increase of field β exceeds 1. Interestingly, irrespective of the field range β is always greater than 1 for $P \geqslant 0.68$ GPa. More surprisingly, β even exceeds *2* at 1.1 GPa. These results demonstrate that collective pinning of vortices may be robust at high magnetic fields and high-pressure regimes in Re_6Hf.

According to the collective pinning theory, the pinning of vortices arises from two processes. One is the pinning due to the spatial variation in the mean free path, known as δl pinning, and the other is due to the spatial variation of random distribution of T_c, called δT_c pinning. This theory predicts $J_c(t)/J_c(0) \propto (\frac{(1-t^2)^{\frac{5}{2}}}{(1+t^2)^{\frac{1}{2}}})$ for δl pinning, whereas for δT_c pinning, $J_c(t)/J_c(0) \propto (\frac{(1-t^2)^{\frac{7}{6}}}{(1+t^2)^{\frac{5}{6}}})$, where $t\ (= T/T_c)$ is reduced temperature. Figure 9 shows that the experimental data at 0 and 0.33 GPa fits well with the theoretical δT_c pinning model at different magnetic fields. This reveals that the δT_c pinning is more dominant at ambient and lower applied P. At 0.68 GPa, the experimental data lies in between the δT_c and δl pinning curves, suggesting the coexistence of $\delta T_c + \delta l$ pinning. With a further increase of P to 1.10 GPa, the pinning behavior changes completely to a δl pinning mechanism. A similar chemical and external P induced change in flux pinning mechanism has also been reported on various superconductors such as MgB_2, $NbSe_2$, and pnictides, respectively [58,64–67]. These results clearly show that P can tune the pinning mechanism from δT_c pinning to δl pinning in Re_6Hf. Here we would like to mention that the δT_c and δl pinning are directly proportional to coherence length ξ and $1/\xi^2$, respectively. In fact, this observation of a crossover pinning mechanism from δT_c to δl with increasing pressure is consistent with the increasing ξ behavior estimated from $\rho(T, H, P)$ measurements [Fig. 6(c)].

Next we study the magnetic field dependence of the flux pinning force $F_p(H) = \mu_0 H \times J_c(H)$ at different pressures based on the Dew-Hughes model for a superconductor [68]. The scaling behavior of the pinning force density, $f(h) = Ah^m(1-h)^n + Bh^p(1-h)^q$, where $f(h) = (\frac{F_p}{F_p^{\max}})$ and $h = (\frac{H}{H_{\rm irr}^k})$ is a normalized pinning force density and reduced magnetic field and $(m,\ n)$, and $(p,\ q)$ are scaling constants used to describe the nature of the pinning mechanism of the sample. The $H_{\rm irr}^k$ at various temperatures is estimated by linearly extrapolating the $J^{0.5}H^{0.25}$ vs H curve towards zero. From the analysis of Kramer's plot [69], the power exponent $(p,\ q)$ becomes (0.5, 2), (1, 2), and (0.5, 1), which indicates the surface boundary pinning, point pinning, and volume pinning, respectively. Normalized magnetic field $(h \sim H/H_{\rm irr}^k)$ dependence of pinning force density $[f = (\frac{F_p}{F_p^{\max}})]$ at various temperatures with fixed applied P is shown in Fig. 10. The Dew-Hughes model, well fitted with the experimental data $(m,\ n)$ and $(p,\ q)$, is $(0.76 \pm 0.04, 1.32 \pm 0.07)$ and $(0.86 \pm 0.21, 2.46 \pm 0.46)$, respectively, at 2 K, revealing the coexistence of both volume and grain boundary pinning at ambient

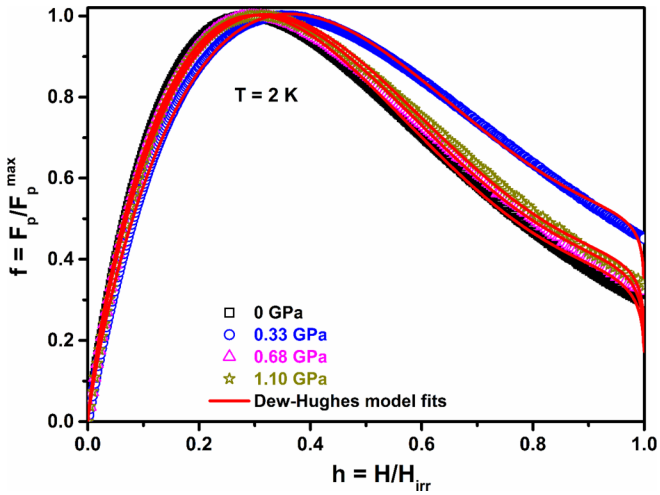

FIG. 10. Normalized magnetic field dependence of normalized pinning force at 2 K with various applied P, and solid lines represent the fitting of the Dew-Hughes model to describe the nature of flux pinning.

P. The extracted power exponents [(m, n) and (p, q)] from the fitting analysis show (0.87 ± 0.04, 2.07 ± 0.08) and (0.81 ± 0.09, 2.60 ± 0.06) at 0.33 GPa, (0.86 ± 0.04, 2.38 ± 0.09) and (0.78 ± 0.09, 2.68 ± 0.06) at 0.68 GPa, and (0.86 ± 0.04, 2.39 ± 0.37) and (0.78 ± 0.13, 3.10 ± 0.09) at 1.10 GPa. With the application of P (∼0.33 GPa), the volume pinning is completely changed to point pinning, revealing that the point pinning center is enhanced with the application of external P. Furthermore, the surface pinning is more dominant than the point pinning above ∼0.33 GPa, possibly due to the relocation of grain boundaries in this polycrystalline sample.

We measured the pressure-dependent XRD pattern of Re_6Hf at room temperature using a Rigaku diffractometer to check for the possibility of any pressure-induced structural transition as shown in Fig. S3 of the Supplemental Material [44]. The powder diffraction pattern was processed by the CRYSALIS PRO (Rigaku Oxford diffraction) software, and the crystal structure and lattice parameters are confirmed using the SHELXT and SHELXL-2018/3 methods. With pressurization the peak position moves towards a higher 2θ angle, suggesting shrinkage of the lattice parameters. In Fig. 11 we plot the calculated unit-cell volume and lattice parameter. With pressure up to 18.01 GPa, the lattice parameters and unit-cell volume are compressed by 1% and 3%, respectively. The smooth variation of these structural parameters rules out a structural transition up to 18.01 GPa. Furthermore, we did not detect any discernible new peak even at ∼18 GPa, which can signal the occurrence of a structural change. The bulk modulus (B_0) is calculated from the unit-cell volume using the first-order Birch-Murnaghan equation of state [70,71], $P = \frac{B_0}{B_0'}[(\frac{V_0}{V})^{B_0'} - 1]$. The large value of high $B_0 =$ 333.63 GPa suggests that Re_6Hf exhibits poor compressibility. This may be one reason for the modest change of T_c with pressure.

The calculated electronic band structure using density functional theory is shown in Figs. 12(a) and 12(b). The total density of states (DOS) at Fermi level, E_F, together with the site projected partial DOS are shown in Fig. 12(c). In both ambient and high-pressure phases, the bands are crossover the E_F and the DOS is small but finite, underscoring the Re_6Hf to be metallic. The total DOS at the equilibrium volumes as a function of P is displayed in Fig. 12(d). On a closure look at Fig. 12(e), DOS decreases barely up to 10.0 GPa and is followed by a slight decrease thereafter. This observation agrees well with the experimental results of a modest T_c decrease up to 8 GPa. The DOS near the Fermi level is entirely composed of Re and Hf − d bands; however, since the ratio of Re to Hf is 6:1, Re-d bands comprise the majority of the states. In the entire valance band region, in addition to the Hf- and Re-d states Hf-p and s states are predominant compared with the Re-s and p states.

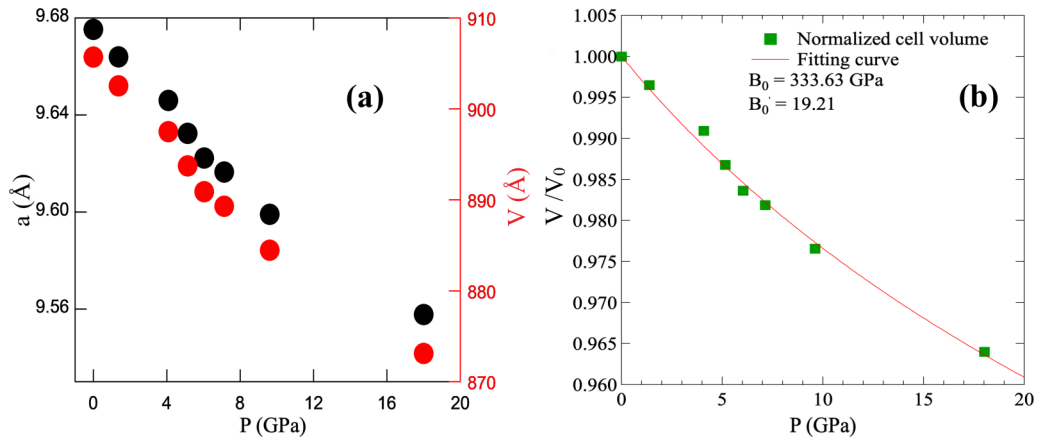

FIG. 11. (a) Pressure dependence of lattice parameters and unit-cell volume. (b) Normalized volume (V/V_0) of the unit cell under P. The red solid line represents the Birch-Murnaghan equation-of-state fit to the data.

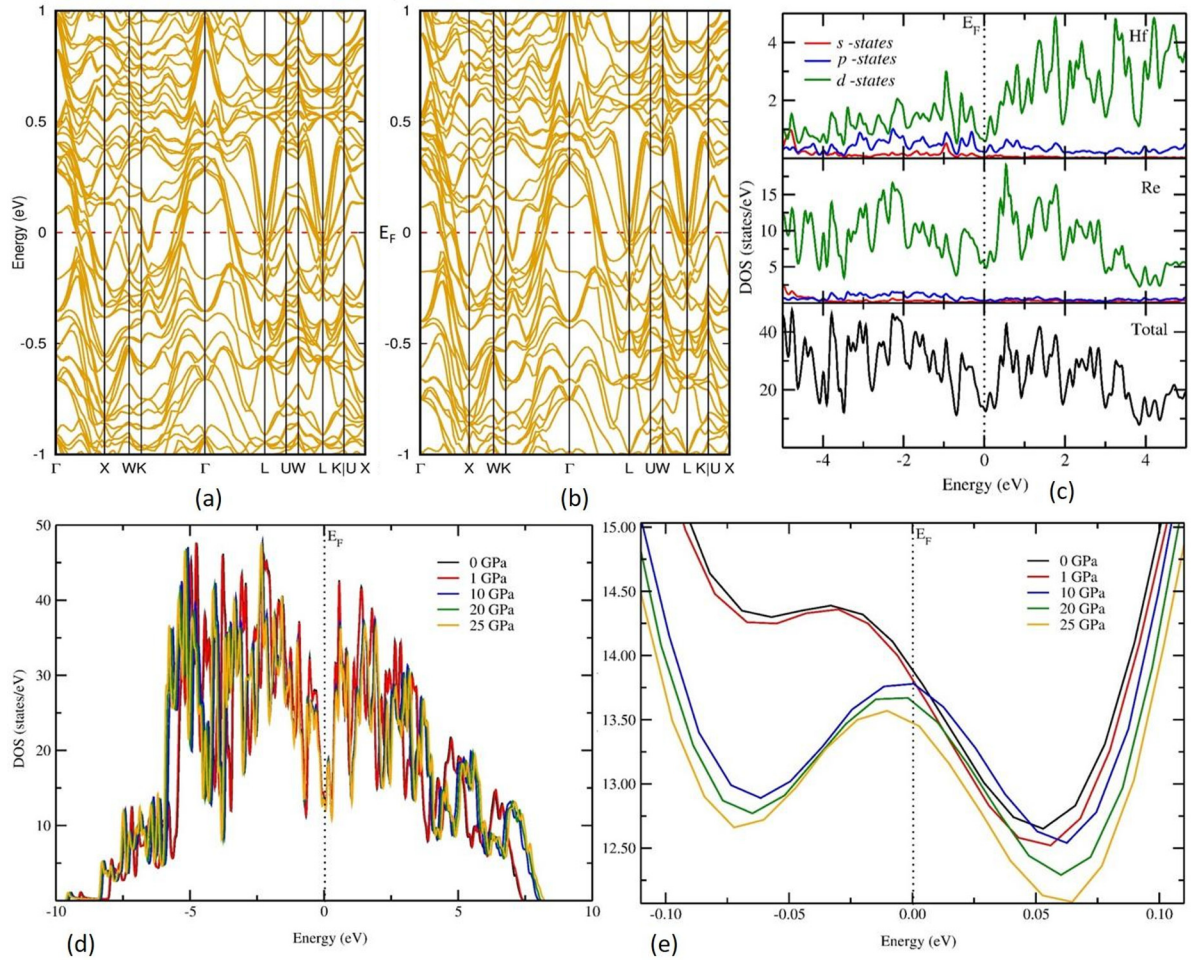

FIG. 12. Calculated electronic band structure for Re_6Hf at ambient pressure at (a) 0 GPa and (b) 10 GPa. (c) Total electronic density of states (DOS) and site and orbital projected DOS, (d) total electronic DOS as a function of pressure, and (e) the magnitude version at the Fermi level (E_F) are shown for Re_6Hf. GGA and PW91 functional are used for the computation. The Fermi level (E_F) is set to zero.

V. CONCLUSION

In summary, we have investigated the superconducting and structural properties of a polycrystalline noncentrosymmetric superconductor, Re_6Hf. We found that as pressure increases to 8.0 GPa, T_c decreases modestly and the superconducting transition width becomes sharper. Analysis of the structure using XRD under pressure rules out any structural transition and a high value of bulk modulus $B_0 = 333.63$ GPa. However, density functional theory calculations suggest a modest reduction of DOS at Fermi level with pressure, which may be a possible reason for such a small decrease of T_c with pressure. Furthermore, both $H_{c2}(0)$ and $H_{c1}(0)$ decrease slightly from the ambient pressure value as pressure increases to 2.5 GPa. In addition, analysis of $\rho(T, H)$ using TAFF of vortices revealed a double linearity field dependence of activation energy of vortices $U_0(H)$, confirming the coexistence of single and collective pinning vortex states. Consistently, analysis of critical current density using the collective pinning theory showed the transformation of δT_c to δl pinning as pressure increases, possibly due to migration of grain boundaries.

ACKNOWLEDGMENTS

S.M. thanks SERB for the financial support to visit ISSP, The University of Tokyo, Japan, through OVDF, and acknowledges the ISSP for providing the experimental facilities during the visit, and thanks Dr. S. Nagasaki, ISSP, The University of Tokyo, Japan, for her continuous support with regard to the cryogenic measurements. S.A. acknowledges SERB, DST (FIST), TANSCHE, UGC-DAE-CSR, Indore, DAE-BRNS, and RUSA 2.0. Y.U. acknowledges JSPS KAKENHI Grant No. JP19H00648. M.K. thanks the UGC-RGNF for the meritorious research fellowship. R.P.S. acknowledges the Science and Engineering Research Board, Government of India, for Core Research Grant No. CRG/2019/001028. P.V. gratefully acknowledges the Research Council of Norway for providing the computer time (under Projects No. NN2875k and No. NS2875k) at the Norwegian supercomputer facility.

[1] E. Bauer, G. Hilscher, H. Michor, C. Paul, E. W. Scheidt, A. Gribanov, Y. Seropegin, and H. Noe, Heavy Fermion Superconductivity and Magnetic Order in Noncentrosymmetric $CePt_3Si$, Phys. Rev. Lett. **92**, 027003 (2004).

[2] P. A. Frigeri, D. F. Agterberg, and M. Sigrist, Spin susceptibility in superconductors without inversion symmetry, New J. Phys. **6**, 115 (2004).

[3] M. Yogi, Y. Kitaoka, S. Hashimoto, T. Yasuda, R. Settai, T. D. Matsuda, Y. Haga, Y. Ōnuki, P. Rogl, and E. Bauer, Evidence for a Novel State of Superconductivity in Noncentrosymmetric $CePt_3Si$: A ^{195}Pt-NMR Study, Phys. Rev. Lett. **93**, 027003 (2004).

[4] N. Kimura, K. Ito, H. Aoki, S. Uji, and T. Terashima, Extremely High Upper Critical Magnetic Field of the Noncentrosymmetric Heavy Fermion Superconductor $CeRhSi_3$, Phys. Rev. Lett. **98**, 197001 (2007).

[5] R. Settai, Y. Miyauchi, T. Takeuchi, F. Lévy, I. Sheikin, and Y. Ōnuki, Huge upper critical field and electronic instability in pressure-induced superconductor $CeIrSi_3$ without inversion symmetry in the crystal structure, J. Phys. Soc. Japan **77**, 073705 (2008).

[6] R. Settai, I. Sugitani, Y. Okuda, A. Thamizhavel, M. Nakashima, Y. Ōnuki, and H. Harima, Pressure-induced superconductivity in without inversion symmetry, J. Magn. Magn. Mater. **310**, 844 (2007).

[7] F. Honda, I. Bonalde, S. Yoshiuchi, Y. Hirose, T. Nakamura, K. Shimizu, R. Settai, and Y. Ōnuki, Pressure-induced superconductivity in non-centrosymmetric compound $CeIrGe_3$, Physica C **470**, S543 (2010).

[8] T. Akazawa, H. Hidaka, H. Kotegawa, T. C. Kobayashi, T. Fujiwara, E. Yamamoto, Y. Haga, R. Settai, and Y. Ōnuki, Pressure-induced superconductivity in UIr, J. Phys. Soc. Japan **73**, 3129 (2004).

[9] Y. Okuda, Y. Miyauchi, Y. Ida, Y. Takeda, C. Tonohiro, Y. Oduchi, T. Yamada, N. Duc Dung, T. D. Matsuda, Y. Haga, T. Takeuchi, M. Hagiwara, K. Kindo, H. Harima, K. Sugiyama, R. Settai, and Y. Ōnuki, Magnetic and superconducting properties of $LaIrSi_3$ and $CeIrSi_3$ with the non-centrosymmetric crystal structure, J. Phys. Soc. Japan **76**, 044708 (2007).

[10] I. Sugitani, Y. Okuda, H. Shishido, T. Yamada, A. Thamizhavel, E. Yamamoto, T. D. Matsuda, Y. Haga, T. Takeuchi, and R. Settai, Pressure-induced heavy-fermion superconductivity in antiferromagnet $CeIrSi_3$ without inversion symmetry, J. Phys. Soc. Japan **75**, 043703 (2006).

[11] T. Kawai, H. Muranaka, M.-A. Measson, T. Shimoda, Y. Doi, T. D. Matsuda, Y. Haga, G. Knebel, G. Lapertot, D. Aoki, J. Flouquet, T. Takeuchi, R. Settai, and Y. Ōnuki, Magnetic and superconducting properties of $CeTX_3$ (T: transition metal and X: Si and Ge) with non-centrosymmetric crystal structure, J. Phys. Soc. Japan **77**, 064716 (2008).

[12] R. Settai, T. Takeuchi, and Y. Ōnuki, Recent advances in Ce-based heavy-fermion superconductivity and Fermi surface properties, J. Phys. Soc. Japan **76**, 051003 (2007).

[13] N. Kimura, K. Ito, K. Saitoh, Y. Umeda, H. Aoki, and T. Terashima, Pressure-Induced Superconductivity in Noncentrosymmetric Heavy-Fermion $CeRhSi_3$, Phys. Rev. Lett. **95**, 247004 (2005).

[14] N. D. Mathur, F. M. Grosche, S. R. Julian, I. R. Walker, D. M. Freye, R. K. W. Haselwimmer, and G. G. Lonzarich, Magnetically mediated superconductivity in heavy fermion compounds, Nature (London) **394**, 39 (1998).

[15] S. Katano, H. Nakagawa, K. Matsubayashi, Y. Uwatoko, H. Soeda, T. Tomita, and H. Takahashi, Anomalous pressure dependence of the superconductivity in noncentrosymmetric $LaNiC_2$: Evidence of strong electronic correlations, Phys. Rev. B **90**, 220508(R) (2014).

[16] S. Katano, K. Shibata, K. Nakashima, and Y. Matsubara, Magnetic impurity effects on the superconductivity of noncentrosymmetric $LaNiC_2$: Ce substitution for La, Phys. Rev. B **95**, 144502 (2017).

[17] P. Badica, T. Kondo, and K. Togano, Superconductivity in a new pseudo-binary $Li_2B(Pd_{1-x}Pt_x)_3$ ($x = 0$–1) boride system, J. Phys. Soc. Japan **74**, 1014 (2005).

[18] M. Nishiyama, Y. Inada, and G. Q. Zheng, Spin Triplet Superconducting State Due to Broken Inversion Symmetry in Li_2Pt_3B, Phys. Rev. Lett. **98**, 047002 (2007).

[19] S. Arumugam, N. Subbulakshmi, K. Manikandan, M. Kannan, D. A. Mayoh, M. R. Lees, and G. Balakrishnan, Investigation of the transport, magnetic and flux pinning properties of the noncentrosymmetric superconductor $TaRh_2B_2$ under hydrostatic pressure, Physica C **571**, 1353586 (2020).

[20] D. A. Mayoh, A. D. Hillier, K. Götze, D. M. K. Paul, G. Balakrishnan, and M. R. Lees, Multigap Superconductivity in Chiral Noncentrosymmetric $TaRh_2B_2$, Phys. Rev. B **98**, 014502 (2018).

[21] E. M. Carnicom, W. Xie, T. Klimczuk, J. Lin, K. Górnicka, Z. Sobczak, N. P. Ong, and R. J. Cava, $TaRh_2B_2$ and $NbRh_2B_2$: Superconductors with a Chiral Noncentrosymmetric Crystal Structure, Sci. Adv. **4**, eaar7969 (2018).

[22] R. Jha, R. Goyal, P. Neha, V. K. Maurya, A. K. Srivastava, A. Gupta, S. Patnaik, and V. P. S. Awana, Weak Ferromagnetism in a Noncentrosymmetric BiPd 4 K Superconductor, Supercond. Sci. Technol. **29**, 025008 (2016).

[23] B. Joshi, A. Thamizhavel, and S. Ramakrishnan, Superconductivity in noncentrosymmetric BiPd, Phys. Rev. B **84**, 064518 (2011).

[24] Y. Nishikubo, K. Kudo, and M. Nohara, Superconductivity in the honeycomb-lattice pnictide SrPtAs, J. Phys. Soc. Japan **80**, 055002 (2011).

[25] P. K. Biswas, H. Luetkens, T. Neupert, T. Stürzer, C. Baines, G. Pascua, A. P. Schnyder, M. H. Fischer, J. Goryo, M. R. Lees, H. Maeter, F. Brückner, H.-H. Klauss, M. Nicklas, P. J. Baker, A. D. Hillier, M. Sigrist, A. Amato, and D. Johrendt, Evidence for superconductivity with broken time-reversal symmetry in locally noncentrosymmetric SrPtAs, Phys. Rev. B **87**, 180503(R) (2013).

[26] R. P. Singh, A. D. Hillier, B. Mazidian, J. Quintanilla, J. F. Annett, D. M. Paul, G. Balakrishnan, and M. R. Lees, Detection of Time-Reversal Symmetry Breaking in the Noncentrosymmetric Superconductor Re_6Zr Using Muon-Spin Spectroscopy, Phys. Rev. Lett. **112**, 107002 (2014).

[27] D. Singh, K. P. Sajilesh, J. A. T. Barker, D. M. K. Paul, A. D. Hillier, and R. P. Singh, Time-reversal symmetry breaking in the noncentrosymmetric superconductor Re_6Ti, Phys. Rev. B **97**, 100505(R) (2018).

[28] D. A. Mayoh, J. A. T. Barker, R. P. Singh, G. Balakrishnan, D. M. Paul, and M. R. Lees, Superconducting and normal-state properties of the noncentrosymmetric superconductor Re_6Zr, Phys. Rev. B **96**, 064521 (2017).

[29] J. A. T. Barker, B. D. Breen, R. Hanson, A. D. Hillier, M. R. Lees, G. Balakrishnan, D. M. K. Paul, and R. P. Singh, Superconducting and normal-state properties of the noncentrosymmetric superconductor Re_3Ta, Phys. Rev. B **98**, 104506 (2018).

[30] T. Shang, G. M. Pang, C. Baines, W. B. Jiang, W. Xie, A. Wang, M. Medarde, E. Pomjakushina, M. Shi, and J. Mesot, Nodeless superconductivity and time-reversal symmetry breaking in the noncentrosymmetric superconductor $Re_{24}Ti_5$, Phys. Rev. B **97**, 020502 (2018).

[31] C. S. Lue, H. F. Liu, C. N. Kuo, P. S. Shih, J.-Y. Lin, Y. K. Kuo, M. W. Chu, T.-L. Hung, and Y. Y. Chen, Investigation of normal and superconducting states in noncentrosymmetric $Re_{24}Ti_5$, Supercond. Sci. Technol. **26**, 055011 (2013).

[32] T. Shang, M. Smidman, S. K. Ghosh, C. Baines, L. J. Chang, D. J. Gawryluk, J. A. T. Barker, R. P. Singh, D. M. K. Paul, G. Balakrishnan, E. Pomjakushina, M. Shi, M. Medarde, A. D. Hillier, H. Q. Yuan, J. Quintanilla, J. Mesot, and T. Shiroka, Time-Reversal Symmetry Breaking in Re-Based Superconductors, Phys. Rev. Lett. **121**, 257002 (2018).

[33] A. B. Karki, Y. M. Xiong, N. Haldolaarachchige, S. Stadler, I. Vekhter, P. W. Adams, D. P. Young, W. A. Phelan, and J. Y. Chan, Physical properties of the noncentrosymmetric superconductor $Nb_{0.18}Re_{0.82}$, Phys. Rev. B **83**, 144525 (2011).

[34] D. Singh, J. A. T. Barker, A. Thamizhavel, D. M. K. Paul, A. D. Hillier, and R. P. Singh, Time-reversal symmetry breaking in the noncentrosymmetric superconductor Re_6Hf: Further evidence for unconventional behavior in the α-Mn family of materials, Phys. Rev. B **96**, 180501(R) (2017).

[35] J. Yang, Y. Guo, H. Wang, and B. Chen, Fe substitution and pressure effects on superconductor Re_6Hf, Solid State Commun. **272**, 12 (2018).

[36] D. Singh, A. D. Hillier, A. Thamizhavel, and R. P. Singh, Superconducting properties of the noncentrosymmetric superconductor Re_6Hf, Phys. Rev. B **94**, 054515 (2016).

[37] N. Mori, H. Takahashi, and N. Takeshita, Low-temperature and high-pressure apparatus developed at ISSP, University of Tokyo, High Press. Res. **24**, 225 (2004).

[38] G. Kresse and J. Furthmüller, Efficient iterative schemes for ab initio total-energy calculations using a plane-wave basis set, Phys. Rev. B **54**, 11169 (1996).

[39] G. Kresse and D. Joubert, From ultrasoft pseudopotentials to the projector augmented-wave method, Phys. Rev. B **59**, 1758 (1999).

[40] P. E. Blöchl, Projector augmented-wave method, Phys. Rev. B **50**, 17953 (1994).

[41] G. Lingannan, B. Joseph, P. Vajeeston, C. N. Kuo, C. S. Lue, G. Kalaiselvan, P. Rajak, and S. Arumugam, Pressure-dependent modifications in the $LaAuSb_2$ charge density wave system, Phys. Rev. B **103**, 195126 (2021).

[42] P. Vinet, J. H. Rose, J. Ferrante, and J. R. Smith, Universal features of the equation of state of solids, J. Phys.: Condens. Matter **1**, 1941 (1989).

[43] C. J. Pickard and R. J. Needs, Ab initio random structure searching, J. Phys.: Condens. Matter **23**, 053201 (2011).

[44] See Supplemental Material at http://link.aps.org/supplemental/10.1103/PhysRevB.105.224505 for further information regarding the Re_6Hf. Which are, the change in five quadrant field dependence of magnetization hysteresis at 2 K under different pressures 0, 0.33, 0.68 and 1.10 GPa (Figure S1); Field dependence of magnetization (two quadrant) for various temperatures below superconducting T_c at each pressure (Figure S2); Powder XRD pattern for various pressures up to 18.01 GPa using Diamond Anvil Cell and powder XRD pattern (outside of pressure cell) at ambient pressure (Figure S3).

[45] C. L. B. Shuddemagen, The demagnetizing factors for cylindrical iron rods, Proc. Am. Acad. Arts Sci. **43**, 185 (1907).

[46] C. R. H. Bahl, Estimating the demagnetization factors for regular permanent magnet pieces, AIP Adv. **11**, 075028 (2021).

[47] E. H. Brandt, Irreversible magnetization of pin-free type-II superconductors, Phys. Rev. B **60**, 11939 (1999).

[48] N. R. Werthamer, E. Helfand, and P. C. Hohenberg, Temperature and purity dependence of the superconducting critical field, H_{c2}. III. Electron spin and spin-orbit effects, Phys. Rev. **147**, 295 (1966).

[49] A. M. Clogston, Upper Limit for the Critical Field in Hard Superconductors, Phys. Rev. Lett. **9**, 266 (1962).

[50] B. S. Chandrasekhar, A note on the maximum critical field of high-field superconductors, Appl. Phys. Lett. **1**, 7 (1962).

[51] M. Schossmann and J. P. Carbotte, Pauli limiting of the upper critical magnetic field, Phys. Rev. B **39**, 4210 (1989).

[52] K. Maki, Effect of Pauli paramagnetism on magnetic properties of high-field superconductors, Phys. Rev. **148**, 362 (1966).

[53] W. J. Choi, Y. I. Seo, D. Ahmad, and Y. S. Kwon, Thermal activation energy of 3D vortex matter in $NaFe_{1-x}Co_xAs$ (x = 0.01, 0.03 and 0.07) single crystals, Sci. Rep. **7**, 10900 (2017).

[54] T. T. M. Palstra, B. Batlogg, L. F. Schneemeyer, and J. V. Waszczak, Thermally Activated Dissipation in $Bi_{2.2}Sr_2Ca_{0.8}Cu_2O_{8+\delta}$, Phys. Rev. Lett. **61**, 1662 (1988).

[55] C. P. Bean, Magnetization of Hard Superconductors, Phys. Rev. Lett. **8**, 250 (1962).

[56] C. P. Bean, Magnetization of high-field superconductors, Rev. Mod. Phys. **36**, 31 (1964).

[57] S. Arumugam, M. Krishnan, K. Ishigaki, J. Gouchi, R. Pervin, G. K. Selvan, P. M. Shirage, and Y. Uwatoko, Enhancement of superconducting properties and flux pinning mechanism on $Cr_{0.0005}NbSe_2$ single crystal under hydrostatic pressure, Sci. Rep. **9**, 347 (2019).

[58] K. Manikandan, R. Pervin, C. Saravanan, M. Sathiskumar, N. Chakraborty, P. M. Shirage, S. Mondal, V. Srihari, H. K. Poswal, and S. Arumugam, Influence of pressure on the transport, magnetic, and structural properties of superconducting $Cr_{0.0009}NbSe_2$ single crystal, RSC Adv. **10**, 13112 (2020).

[59] N. Subbulakshmi, G. Kalaiselvan, K. Manikandan, R. Thiyagarajan, and S. Arumugam, Hydrostatic pressure effect on superconductivity and vortex pinning mechanism of $Sr(Fe_{0.88}Co_{0.12})_2As_2$ single crystal, Physica C **563**, 22 (2019).

[60] M. Murakami, M. Morita, K. Doi, and K. Miyamoto, A new process with the promise of high J_c in oxide superconductors, Jpn. J. Appl. Phys. **28**, 1189 (1989).

[61] M. Murakami, M. Morita, and N. Koyama, Magnetization of a $YBa_2Cu_3O_7$ crystal prepared by the quench and melt growth process, Jpn. J. Appl. Phys. **28**, L1125 (1989).

[62] G. Blatter, M. V. Feigel'man, V. B. Geshkenbein, A. I. Larkin, and V. M. Vinokur, Vortices in high-temperature superconductors, Rev. Mod. Phys. **66**, 1125 (1994).

[63] V. Pan, Y. Cherpak, V. Komashko, S. Pozigun, C. Tretiatchenko, A. Semenov, E. Pashitskii, and A. V. Pan, Supercurrent transport in $YBa_2Cu_3O_{7-\delta}$ epitaxial thin films in a dc magnetic field, Phys. Rev. B **73**, 054508 (2006).

[64] M. Krishnan, R. Pervin, K. S. Ganesan, K. Murugesan, G. Lingannan, A. K. Verma, P. M. Shirage, and A. Sonachalam, Pressure assisted enhancement in superconducting properties of Fe substituted $NbSe_2$ single crystal, Sci. Rep. **8**, 1251 (2018).

[65] B. Shabbir, X. L. Wang, S. R. Ghorbani, S. X. Dou, and F. Xiang, Hydrostatic pressure induced transition from δT_c to δl pinning mechanism in MgB_2, Supercond. Sci. Technol. **28**, 055001 (2015).

[66] S.-G. Jung, J.-H. Kang, E. Park, S. Lee, J.-Y. Lin, D. A. Chareev, A. N. Vasiliev, and T. Park, Enhanced critical current density in the pressure-induced magnetic state of the high-temperature superconductor FeSe, Sci. Rep. **5**, 16385 (2015).

[67] M. Shahbazi, X. L. Wang, K. Y. Choi, and S. X. Dou, Flux pinning mechanism in $BaFe_{1.9}Ni_{0.1}As_2$ single crystals: Evidence for fluctuation in mean free path induced pinning, Appl. Phys. Lett. **103**, 032605 (2013).

[68] D. Dew-Hughes, Flux pinning mechanisms in Type II superconductors, Philos. Mag. A **30**, 293 (1974).

[69] E. J. Kramer, Scaling laws for flux pinning in hard superconductors, J. Appl. Phys. **44**, 1360 (1973).

[70] F. Birch, Finite elastic strain of cubic crystals, Phys. Rev. **71**, 809 (1947).

[71] R. S. Kumar, A. L. Cornelius, and J. L. Sarrao, Compressibility of Ce $M\text{In}_5$ and Ce_2MIn_8 (M = Rh, Ir, and Co) compounds, Phys. Rev. B **70**, 214526 (2004).